Automation in Construction 101 (2019) 179–189

Contents lists available at ScienceDirect

Automation in Construction

journal homepage: www.elsevier.com/locate/autcon

Printability, accuracy and strength of geopolymer made using powder-based 3D printing for construction applications

Ming Xia, Behzad Nematollahi**, Jay Sanjayan*

Center for Sustainable Infrastructure, Faculty of Science, Engineering and Technology, Swinburne University of Technology, Hawthorn, Australia

ARTICLE INFO

Keywords:
Geopolymer
Fly ash
Construction
Powder-based 3D printing
Compressive strength
Additive manufacturing
Dimensional accuracy
Post-processing

ABSTRACT

The authors of this study have recently succeeded to develop geopolymer materials using slag only formulations for the requirements and demands of commercially available powder-based 3D printers. In this study, the formulation is extended to fly ash and slag combinations so that to expand the scope of geopolymer materials that can be used in the commercially available powder-based 3D printers for construction applications. The quantitative influence of fly ash content on the printability characteristics (i.e., depositability and wettability) of the geopolymer powder, as well as the linear dimensional accuracy and compressive strength of the printed specimens were investigated. The effect of type of alkaline solution used for post-processing on the linear dimensional accuracy and compressive strength of the post-processed specimens were also evaluated. The results indicated that the increase in fly ash content had no effect on the powder depositability, but adversely affected the powder wettability, linear dimensional accuracy and compressive strength of the printed specimens. The minimum slag content required to prepare fly ash/slag blended geopolymer powder for powder-based 3D concrete printing process is 50 wt%. The post-processing significantly increased the compressive strength. The post-processed specimens printed with 50 wt% slag/50 wt% fly ash powder exhibited a 7-day compressive strength of up to 25 MPa, which is sufficiently high for many construction applications.

1. Introduction

Additive manufacturing (AM), commonly known as three-dimensional (3D) printing, creates components in a layer-wise form directly from digital model data. Several industries including aerospace, automotive, biomedical have already explored the benefits of adapting this technology as an integral part of their product manufacturing process [1].

Recently, 3D printing is receiving significant attention in the construction industry owing to its potential use for direct construction of buildings and other complex structures of virtually any shape without the use of expensive formwork [2–12].

Two different 3D printing techniques are used in the construction industry. One of which is known as powder-based 3D concrete printing (3DCP) technique that is a typical AM process capable of making complex structures with subtle details and intricate shapes through jetting a liquid binder (or "Ink") selectively through the nozzle(s) on a layer of printable powder, causing the powder particles to bind to each other. One of the advantages of this technique is that structures with overhang parts can be printed without the necessity of a support structure. Examples of technologies developed based on the powder-based 3DCP include D-Shape [13] and Emerging Objects [14].

The primary benefit offered by 3DCP is the high flexibility in design. Complex geometries that were previously difficult or impossible to produce using conventional manufacturing process are now capable of being built via 3DCP techniques. Difficulties in meeting stringent requirements regarding dimensional and shape accuracy have become a critical issue need to be overcome before a more widespread application of 3DCP techniques [15,16].

Generally, in the construction industry, the demand for accuracy is not as high as in mechanical components. However, the powder-based 3DCP is likely to be used for highly detailed ornamental shapes where the high accuracy will be demanded, depending on the size and shape of the components produced.

Extensive research work in the 3DCP field has been conducted to address issues such as developing suitable equipment, developing and testing printable materials and designing feasible structural reinforcement. A limited number of research related to the dimensional and shape accuracy has been conducted. Lim et al. [17] used a laser scanning technique to evaluate the manufacturing tolerances of extrusion-

* Corresponding author at: Swinburne University of Technology, Mail 38, FSET, Hawthorn, Victoria 3122, Australia.
** Corresponding author.
E-mail address: jsanjayan@swin.edu.au (J. Sanjayan).

https://doi.org/10.1016/j.autcon.2019.01.013
Received 24 April 2018; Received in revised form 17 December 2018; Accepted 22 January 2019
Available online 10 February 2019
0926-5805/

based 3DCP components against the original CAD model. Authors of this study [18,19] have investigated the effect of printing parameters on the linear dimensional accuracy of powder-based 3D printed specimens.

The powder-based 3DCP technique has the capability to efficiently manufacture building components without the use of expensive formwork. However, the very limited printing materials in powder-based 3DCP prevent this technique to perform at its maximum potential for construction applications [20].

Conventional Portland cement has been considered as the master construction material for its high strength and stability as well as its low cost for over 100 years and will probably be produced and used for at least the next 100 years [21]. However, the setting characteristics of Portland cement limit its use for powder-based 3DCP process. Few studies have reported the use of other types of cementitious materials. For instance, magnesium oxychloride cement (also known as Sorel cement) [13] and fiber reinforced cement polymer [14] were used in D-shape and Emerging Objects, respectively. In addition, Gibbons et al. [22] conducted a preliminary study to investigate the feasibility of using a mixture of polyvinyl alcohol and rapid hardening Portland cement (RHPC) for the powder-based 3DCP process for the manufacture of biomedical implants. The printed specimens exhibited a maximum modulus of rupture of 2.4 MPa after 26-day water immersion at ambient temperature. The low strength of the developed RHPC powder limits its use for construction applications. Maier et al. [23] investigated a mixture of flash-setting calcium aluminate cement (CAC) for powder-based 3D printing to fabricate a bone regeneration scaffold. A compressive strength of up to 20 MPa was reported for the printed specimen after 3-day water immersion.

To broaden the range of printing materials which are suitable for powder-based 3DCP process, the authors of this study have recently succeeded to formulate geopolymer materials which can be used in the commercially available powder-based 3D printers [5,24,25]. Geopolymer [26] is a sustainable alternative binder to Portland cement, which can be produced by alkali activation of industrial by-products (such as fly ash and slag) which are rich in alumina and silica [27,28]. It should be noted that in this paper, the term geopolymer is used in its broad meaning to represent alkali activated cements, although it is understood that some can be alkali-activated slag or fly ash, especially those cured with relatively low alkalinity. This is justified since the term geopolymer has become a common-usage-term for alkali activated cements in the literature [29], even for materials not having full 3D aluminosilicate molecular frameworks.

Compared with Portland cement, geopolymer offers excellent advantages, including (1) geopolymer exhibits substantially superior resistance to fire, sulfate and acid attacks [29], (2) carbon emissions of geopolymer production is about 80% less than Portland cement [30], and (3) the utilization of slag and fly ash in geopolymer is considered to be particularly beneficial, as the disposition of these industrial by-products has always been a global issue. The materials technology research in geopolymer during the last two decades has given us essential knowledge and in-depth understanding of this sustainable construction material. The use of geopolymer in powder-based 3DCP process expands the application of this environmentally friendly material. In the previous study [24], the authors of this paper succeeded in developing a 100% slag-based geopolymer to be used in the commercially available powder-based 3D printers. The printed geopolymer specimens exhibited a compressive strength of up to 16.5 MPa with good dimensional accuracy.

However, fly ash-based geopolymers possess many properties that are better than slag-based geopolymers such as better fire resistance, lower shrinkage and creep properties [29]. Fly ash is more abundantly available, and a large part of it still dumped in landfills in many parts of the world. On the other hand, slag has much better utilization rate and currently most of it consumed in concrete production. Therefore, there are more incentives to use fly ash to produce geopolymer than slag [31,32]. However, fly ash poses a major limitation in that the geopolymer made from fly ash requires high-temperature curing (typically 60 °C) whereas slag-based geopolymer can set at room temperature. Fly ash alone cannot be used in powder-based 3DCP technique because it cannot set at room temperature. Therefore, a minimum amount of slag is necessary to promote setting at room temperature. This study is set out to find the minimum amount of slag required for this purpose and observes the characteristics as slag is reduced in the geopolymer mix. It is intended for broadening the scope of printable geopolymer materials compatible with the powder-based 3DCP process for construction applications.

Table 1
The chemical composition of slag and fly ash (wt%).

Chemical	Component	
	Slag	Fly ash
Al_2O_3	12.37	25.56
SiO_2	32.76	51.11
CaO	44.64	4.30
Fe_2O_3	0.54	12.48
K_2O	0.33	0.70
MgO	5.15	1.45
Na_2O	0.22	0.77
P_2O_5	0.88	0.01
TiO_2	0.51	1.32
MnO	0.15	0.37
SO_3	4.26	0.24
LOI[a]	0.09	0.57

[a] Loss on ignition (unburnt carbon content).

2. Experimental procedures

2.1. Materials and mix proportions

A slag supplied from Independent Cement, Australia and a low calcium fly ash (Class F) supplied from Gladstone power station in Queensland, Australia, were used in this study. The chemical composition and loss on ignition (LOI) of the fly ash and slag determined by X-ray Fluorescence (XRF) are given in Table 1.

Anhydrous sodium metasilicate powder (in the form of bead) supplied by Redox, Australia with the chemical composition of 50.66 wt% Na_2O, 47.00 wt% SiO_2 and 2.34 wt% H_2O was used as the alkaline activator in this study. A high purity silica sand with a median size of 184 μm supplied by TGS Industrial Sand Ltd., Australia was also used in this study.

As presented in Table 2, five geopolymer powders with different slag to fly ash ratios were investigated in this study. To prepare each mix, the alkaline activator beads were firstly ground for 5 min using a planetary ball mill with powder/ball mass ratio of 0.3. Then fly ash, slag, silica sand and the ground activator powder were thoroughly dry mixed in a Hobart mixer to achieve a homogenous mixture (visually assessed).

Different combinations of saturated anhydrous sodium metasilicate, N Grade sodium silicate and sodium hydroxide (NaOH) solutions were used for the post-processing of green samples. Saturated anhydrous

Table 2
Mix proportions of geopolymer precursors.

Mix ID	Geopolymer precursors wt%	
	Slag	Fly ash
S100FA0	100	0
S75FA25	75	25
S50FA50	50	50
S25FA75	25	75
S0FA100	0	100

sodium metasilicate solution was prepared using the anhydrous sodium metasilicate powder and tap water. The N Grade sodium silicate solution was supplied by PQ Australia with a modulus (M_s) of 3.22 (where $M_s = nSiO_2/nNa_2O$, $Na_2O = 8.9$ wt% and $SiO_2 = 28.6$ wt%). The NaOH solution was prepared with a concentration of 8.0 M using NaOH beads of 97% purity supplied by Sigma-Aldrich and tap water.

2.2. Printability characterizations of geopolymer powder

The printability of each geopolymer powder was characterized by measuring the particle size distribution (PSD), true/bulk densities, in-process bed density, powder bed porosity, binder droplet penetration behavior and powders' depositability. Details of the printability characterization process can be found in the authors' previous work [24].

The PSD was determined with a Cilas 1190 laser diffraction particle size distribution analyzer. The true density ($\rho_{true.powder}$) and bulk density ($\rho_{bulk.powder}$) were measured according to Australian standards AS 1774.6 (2013) and AS 1774.2 (2013) respectively. The powder bed porosity (P_{bed}) can be determined by the following equation:

$$P_{bed} = 1 - \frac{\rho_{bed.powder}}{\rho_{true.powder}} \times 100\% \quad (1)$$

where $\rho_{bed.powder}$ is the in-process bed density calculated from the mass and volume of the powder on the build plate.

Fig. 1 schematically illustrates a custom-made apparatus used to assess the binder droplet penetration behavior of each powder which was quantified by three parameters, namely droplet penetration time (t_p), droplet penetrating depth (d_p) and droplet spreading diameter (φ_p). t_p is the time needed for the droplet to penetrate into the powder bed completely, which was calculated using a high-speed video camera. The bonded particles in the powder bed were left undisturbed for 2 h to solidify and d_p and φ_p of which were then measured using a digital caliper. For each powder mix, the t_p, d_p and φ_p measurements were conducted 10 times.

The depositability of powders was analyzed by using a digital image processing technique. As illustrated in Fig. 2, the prepared powder bed was illuminated by a light source at a 45-degree angle to the powder surface and photographed using a high-resolution camera mounted with a macro lens. The powders' surfaces were visualized using interactive 3D surface plots in ImageJ software. The interactive 3D surface plots plug-in can transfer the luminance of an image as height for the plot for assessing the roughness of a surface. The 3D surface plots are displayed in the colour schemes of "Fire look-up-table". The plots apply the drawing modes of a filled surface with a grid size of 1024 and a smoothing of 20.0. As can be seen in Fig. 2(b) and (c), a significant difference between a smooth surface and a rough surface can be revealed by using this image processing method.

2.3. Powder-based 3DCP process

In this study, the 3D printing process was conducted using a Zprinter® 150 which is a commercial powder-based 3D printer manufactured by *Z*-Corp, USA. The 3D printer has a specified resolution of 300 × 450 dpi, a 185 × 236 × 132 mm build volume and a build speed of 2–4 layers per minutes.

An aqueous solvent (Zb® 63, Z-Corp, USA) was used as the binder during the 3DCP process. The Zb® 63 binder was an aqueous commercial clear solution with the viscosity similar to pure water which does not react with slag and fly ash powder. According to Asadi-Eydivand et al. [33], the composition of Zb® 63 was mainly water with 2-Pyrrolidone. In the powder-based 3DCP process, the binder solution is delivered from binder feeder to the print head and is jetted by nozzles mounted in the HP11 print head (C4810A). The HP11 print head has 304 nozzles with a drop size of 2.5 pL for each nozzle. A binder/volume ratio of 0.24 for the shell section and 0.12 was selected for the core section of the printed structure.

A powder layer thickness of 0.1016 mm was used, and the powder was spread and smoothed by the roller over the powder bed surface. According to Shanjani and Toyserkani [34], for a powder layer thickness 0.1016 mm, the maximum compact pressure occurred in the narrowest gap between the roller and the underneath powder layer was less than 0.9 Pa which did not exceed the load capacity of the green samples.

A 20 mm cube model designed by using SolidWorks® software was used for the printing. After 6 h of drying within the powder bed, de-powdering was performed using compressed air to remove the unbounded powder.

2.4. Post-processing procedure

After the de-powdering process, the printed cubes were divided into two groups. For the first group denoted as "green samples", no further post-processing procedures have been undertaken. For the other group denoted as "post-processed samples", the printed cubes were immersed in three different alkaline solutions and placed in the oven at 60 ± 3 °C for 7 days. The following alkaline solutions were used:

(1) Curing Solution I: composed of saturated anhydrous sodium metasilicate solution with SiO_2/Na_2O molar ratio of 0.9;
(2) Curing Solution II: composed of saturated anhydrous sodium metasilicate solution with SiO_2/Na_2O molar ratio of 0.9 (71.4% *w*/w) and 8.0 M NaOH solution (28.6% w/w);
(3) Curing Solution III: composed of N Grade sodium silicate solution with SiO_2/Na_2O molar ratio of 3.22 (71.4% w/w) and 8.0 M NaOH solution (28.6% w/w).

At the end of the heat curing period, the post-processed samples were removed from the oven and kept undisturbed until being cool.

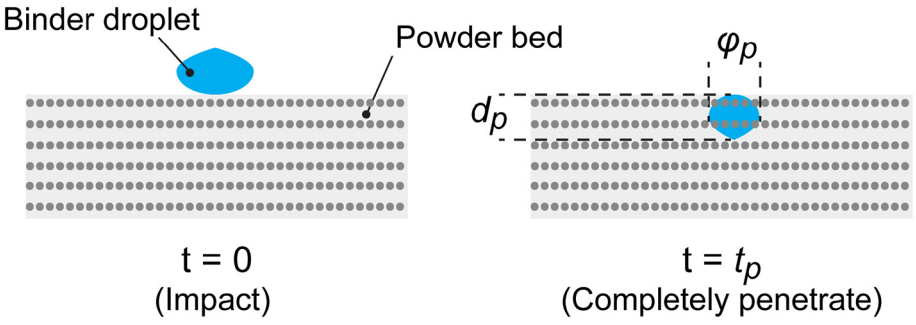

Fig. 1. Schematic illustrations of binder droplet penetration behavior test.

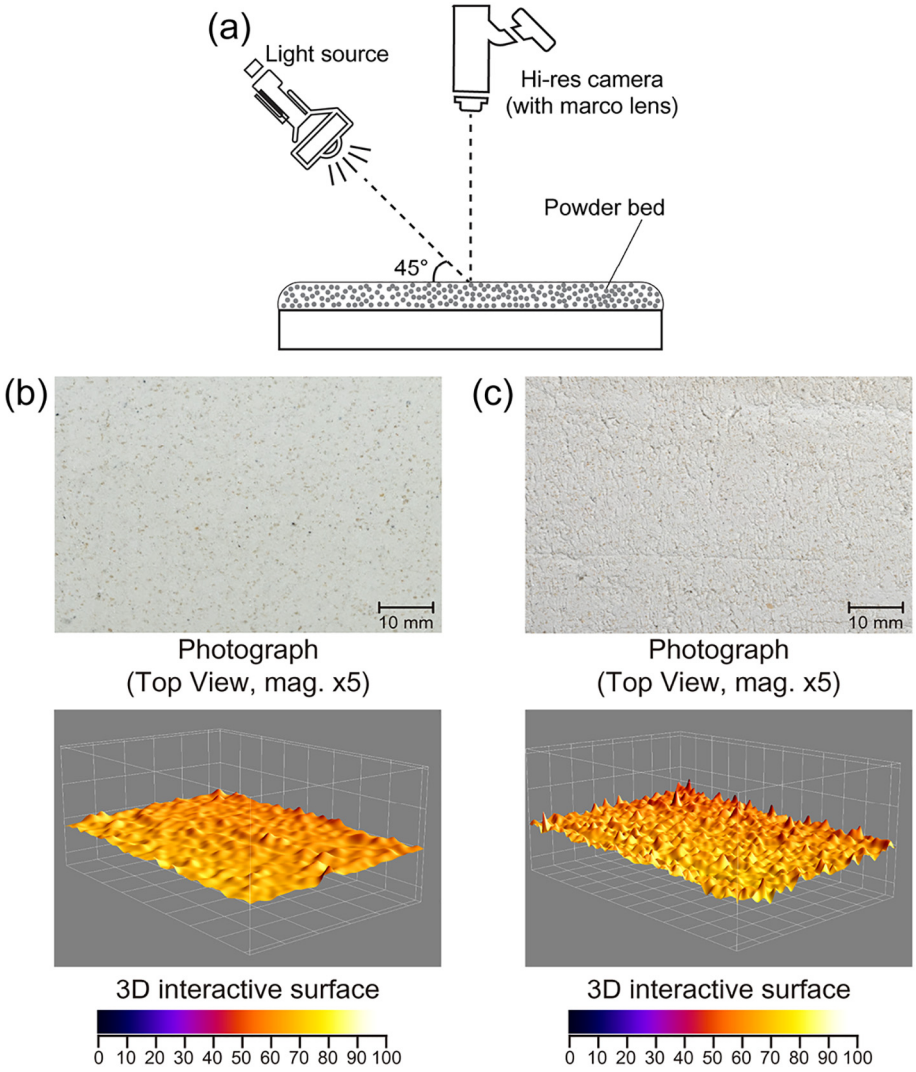

Fig. 2. (a) Schematic illustrations of powder depositability analysis, Photographs and 3D interactive surfaces of (b) smooth surface and (c) rough surface.

Table 3
The particle size of geopolymer powders.

Mix ID	Particle size (μm)		
	D_{10}[a]	D_{50}[b]	D_{90}[c]
S100FA0	1.23	17.24	52.75
S75FA25	1.31	13.17	46.69
S50FA50	1.06	9.21	40.21
S25FA75	0.83	5.88	36.27
S0FA100	0.53	4.94	36.13

[a] 10% of particles are smaller than the size;
[b] 50% of particles are smaller than the size;
[c] 90% of particles are smaller than the size.

2.5. Characterizations of 3D printed specimens

2.5.1. Linear dimensional accuracy

The dimensions of green samples were measured in three directions, namely X-direction (binder jetting direction), Y-direction (powder layer spreading direction) and *Z*-direction (layer stacking direction). The linear dimensional error was calculated using the following equation:

$$Error = L_{actual} - L_{nominal} \quad (2)$$

where L_{actual} is the measured length, whereas L_{nominal} is length of the digital model. A population of 10 samples for each testing direction was used. For each sample three measurements were taken for each testing direction and the mean errors were calculated and used for the assessment of linear dimensional accuracy.

2.5.2. Mechanical property

The compressive strength of both green and post-processed samples in both X-direction and *Z*-direction were measured under load control at the rate of 0.33 MPa/s. A population of 10 samples for each testing direction was tested.

3. Results and discussions

3.1. Powder characteristics

3.1.1. Particle size and particle size distribution

The particle size and PSD of geopolymer powders are presented in Table 3 and Fig. 3, respectively. As shown in Fig. 3, the particle sizes of all geopolymer powders (with different slag to fly ash ratios) range from 0.1 to 100 μm. The raw slag and the raw fly ash used for making the powders have a D_{50} of 12.68 μm and 3.74 μm, respectively. Thus, the relative proportion of particles within the size range of 1–10 μm increased with increasing the fly ash content.

As can be seen in Table 3, the D_{50} of S100FA0 powder (with 100% slag) decreased from 17.24 μm to 4.94 μm for S0FA100 powder (with

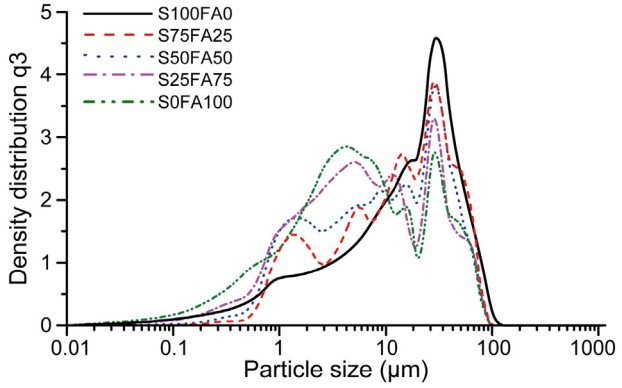

Fig. 3. Particle size distributions of geopolymer powders.

100% fly ash).

In the powder-based 3DCP process, the particle size and PSD are critical for the powder depositability, which enable a smooth and homogeneous powder bed [35,36]. According to Utela et al. [36], the recommended powder particle size for dry deposition is greater than 20 μm. However, in this study visual observations indicated that all geopolymer powders exhibited sufficient surface qualities for the powder-based 3DCP process. This is because the morphology of the powder particles has not been considered in the aforementioned recommended particle size. The fly ash particles are spherical solids [37,38], which can reduce particle interlocking and the resistance to flow.

3.1.2. True/bulk densities, in-process bed density and powder bed porosity

The true/bulk densities, in-process bed density and powder bed porosity of each geopolymer powder are summarized in Table 4.

The increase in the amount of fly ash in the geopolymer powder reduced the true, bulk and in-process bed densities of the powder, but increased the powder bed porosity. However, the effect was not significant. For each geopolymer powder mix, the marginal difference between bulk density and in-process bed density indicates the powder has not been significantly compressed during the powder spreading process.

3.1.3. Binder droplet penetration behavior

Fig. 4 presents the images of typical binder droplet penetration behavior of the geopolymer powders.

The increase of the fly ash content of the geopolymer powder increased the time needed for the binder droplet to penetrate into the powder bed completely. This implies that the powder properties including powder density as well as the size and shape of the particles influence the binder droplet penetration behavior.

After completion of the penetration of the binder droplet into the powder bed, granules were formed within the powder bed. These solid granules had enough green strength for the measurement of d_p and φ_p, except for S0FA100 mix (the geopolymer powder with 100% fly ash). The low reactivity of this geopolymer powder containing 100% fly ash caused the granules to be too weak to withstand the pressure during the de-powdering process. Table 5 summarizes the t_p, d_p and φ_p of each geopolymer powder. The reported values given in this table for each parameter is the average of 20 measurements, and the reported errors are based on 95% confidence level.

Table 4
True/bulk densities, in-process bed density and powder bed porosity of geopolymer powders.

Powder properties	Mix ID				
	S100FA0	S75FA25	S50FA50	S25FA75	S0FA100
True density (g·cm^{-3})	2.81	2.73	2.66	2.59	2.51
Bulk density (g·cm^{-3})	0.78	0.76	0.75	0.72	0.69
In-process bed density (g·cm^{-3})	0.83	0.81	0.78	0.75	0.73
Powder bed porosity (%)	70.4	70.4	70.6	71.0	70.9

As shown in Table 5, the geopolymer powder containing 100% slag (S100FA0) demonstrated the lowest binder droplet penetration time. The longest t_p was for S0FA100 powder containing 100% fly ash, which was 73% longer than that of S100FA0 powder. The higher the fly ash content in the geopolymer powder, the finer the average particle size of the powder, which results in the longer binder droplet penetration time. According to Hapgood [39], changing the particle size will alter the pore structure within the powder bed. Fine powder particles tend to agglomerate, thereby creating a large number of macro voids within the powder bed. The binder liquid has a tendency to flow through micro-voids around the macro-voids, which significantly increases the penetration time. Therefore, the binder droplet penetration time will be longer for geopolymer powder containing more fly ash with a finer average particle size.

As shown in Table 5, the geopolymer powder containing 100% slag (S100FA0) demonstrated the biggest binder droplet spreading diameter (φ_p). The increase of the fly ash content of the geopolymer powder reduced the φ_p. In the powder-based 3DCP process, the binder droplet spreading diameter is an important factor that affects the quality of the printed sample. Either excessive or insufficient spreading diameter compromises the printing accuracy [40]. After impacting the powder bed, the binder droplet spreads out horizontally reaches to its maximum spread diameter in a very short time. According to Nefzaoui et al. [41], φ_p depends on the physicochemical characteristics of the binder droplet and the powder bed surface hydrophilicity. When the surface hydrophilicity of the powder bed is decreased, the horizontal spreading process will be delayed resulting in a lower φ_p [42]. As shown in Fig. 3, the relative proportion of particles within the size range of 1–10 μm increased with increasing the fly ash content. According to Li et al. [43], for the fly ash, particles within the 1–10 μm range exhibited lower wettability than those with size less than 1 μm or more than 10 μm. Therefore, the reduction in surface hydrophilicity may be attributed to the increase in the content of fly ash particles within the size range of 1–10 μm.

On the other hand, the lowest binder droplet penetration depth (d_p) was for the geopolymer powder containing 100% slag (S100FA0). The higher the fly ash content, the higher the d_p of the geopolymer powder. In general, the binder droplet penetration takes place after spreading. For a single binder droplet with a fixed-volume, the smaller the spreading diameter, the higher the penetration depth (i.e., binder droplet has to penetrate deeper into the powder bed to complete the penetration process). Thus, it is reasonable that S100FA0 powder had the lowest d_p, but the biggest φ_p.

It should be pointed out that the interlayer bond strength between layers is probably the most important property in a layer-wise manufacturing process. In the powder-based 3DCP process, adjacent powder layers are combined by the reaction between powder particles and binder liquid. Insufficient binder droplet penetration might cause incompletion of powder-binder reaction between layers, which results in poor green strength of the printed sample. Conversely, excessive binder droplet penetration is also undesirable, because if the binder liquid penetrates too deep within solidified layers, powder/binder reaction may start again, which results in low printing resolution [44].

3.1.4. Depositability of powders

Fig. 5 presents the photographs taken from the powder bed of different geopolymer powders and their corresponding 3D interactive surfaces obtained using the image processing method explained in Section 2. According to Fig. 5, there is no significant difference between the obtained 3D interactive surfaces of different powders, which indicated that all prepared geopolymer powders exhibited similar

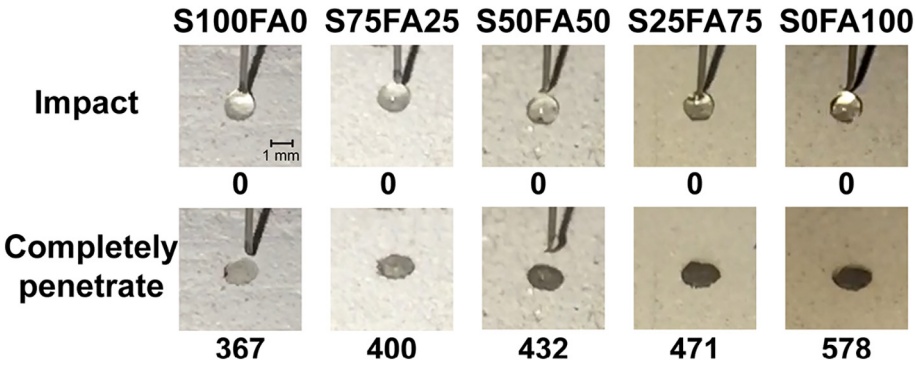

Fig. 4. Images of binder droplet impacting on surfaces of geopolymer powder beds. Note: The numbers below each image indicate the droplet penetration time (ms).

Table 5
Binder droplet penetration behavior results of geopolymer powders.

Mix ID	Binder droplet penetration parameters		
	t_p[a] (ms)	d_p[b] (mm)	φ_p[c] (mm)
S100FA0	335 ± 42	2.10 ± 0.21	1.95 ± 0.16
S75FA25	370 ± 64	2.46 ± 0.22	1.82 ± 0.11
S50FA50	440 ± 57	2.78 ± 0.29	1.72 ± 0.15
S25FA75	490 ± 43	2.90 ± 0.18	1.67 ± 0.16
S0FA100	580 ± 76	—[d]	—[d]

[a] Binder droplet penetration time.
[b] Binder droplet penetration depth.
[c] Binder droplet spreading diameter.
[d] Could not be measured due to the weak strength of granules made with this powder.

depositability.

3.2. Characteristics of 3D printed specimens

Fig. 6 presents the 3D printed cubes using the geopolymer powders with different slag/fly ash ratios. No sample could be printed from the geopolymer powder containing 100% fly ash (S0FA100) due to the low reactivity of this powder with the binder liquid at ambient temperature. Thus, no data is available for S0FA100 powder with regards to the linear dimensional accuracy and compressive strength results.

3.2.1. Linear dimensional accuracy analysis

The primary benefit offered by the powder-based 3DCP process is the capability of producing building component that is detailed and intricate. One of the important factors that define the printability of a newly developed powder system is the printing accuracy. In the construction industry, the question of accuracy is of prime importance for a large variety of applications such as the accuracy of holes on the precast components for bolt/anchor installation. The basic principle for accuracy assessment is to evaluate the degree of deviation between the actual printed specimen and the digital model [15].

Fig. 7 presents the results of linear dimensional accuracy analysis of both green and post-processed samples. It should be noted that S25FA75 samples were dissolved in the curing solutions during the post-processing process. Therefore, no data is available for the linear dimensional accuracy of S25FA75 post-processed samples.

3.2.1.1. Linear dimensional accuracy analysis of green samples. According to Fig. 7, for the green samples the mean error values in all directions were always greater than zero. This indicates that the measured dimensions of the printed cubes in all directions were more than those of the digital model. This is true regardless of the fly ash content.

An anisotropic phenomenon was observed regarding the linear dimensional accuracy of the green samples depending on the directions. The *Z*-direction had the highest mean error and standard deviation values, thereby the lowest linear dimensional accuracy. In addition, the increase of the fly ash content considerably increased the mean error values in the Z-direction. For the green samples, the mean error values in the Z-direction significantly increased from 0.23 mm in S100FA0 powder to 0.38 mm in S25FA75 powder. In other words, the increase of the fly ash content significantly reduced the linear dimensional accuracy of the green samples in the *Z*-direction. This could be attributed to the differences in powder bed structure and level of powder/binder reactivity of the geopolymer powders. As mentioned in Section 3.1.3, when the binder liquid is selectively applied on the powder bed surface, the binder droplet starts to penetrate into the powder bed. If a large number of macro voids are formed within the powder bed, or the reactivity between powder particles and binder liquid is low, only a small amount of binder liquid will be "trapped" within a layer of powder and the excess binder liquid will continue the penetration process [39]. If the excess binder liquid penetrates within the former solidified layers, the powder/binder reaction may start again, which results in distortion between the adjacent layers [45].

On the other hand, the fly ash content had a minor effect on the linear dimensional accuracy in the X-direction and Y-direction, compared with that in the Z-direction. For instance, in the X-direction the mean error values of the green samples in S100FA0 and S25FA75 powders were 0.09 mm and 0.08 mm, respectively. In the Y-direction the corresponding values were 0.12 mm and 0.11 mm, respectively.

Among the three directions, the X-direction had the lowest mean error and standard deviation values, thereby the highest linear dimensional accuracy. This is true regardless of the fly ash content. This might be because the X-direction (i.e., the binder jetting direction) is not affected by the powder spreading, which takes place in the Y-direction [46].

3.2.1.2. Linear dimensional accuracy analysis of post-processed samples. As shown in Fig. 7, for the post-processed samples the mean error values in all directions were also greater than zero, implying that the measured dimensions of the printed cubes in all directions were more than those of the digital model. This is true regardless of the fly ash content and the type of alkaline solution used for the post-processing.

The anisotropic phenomenon still existed regarding the linear dimensional accuracy of the post-processed samples depending on the directions and the type of curing solution. For the samples immersed in Curing Solution I, the mean error values in the X-direction were quite close to those of the green samples. This is true irrespective of the fly ash content. In the Y-direction and *Z*-direction the linear dimensional accuracy appears to be lower than that of the green samples. However, the difference is statistically insignificant.

For the post-processed samples immersed in Curing Solution I, the increase of the fly ash content reduced the linear dimensional accuracy

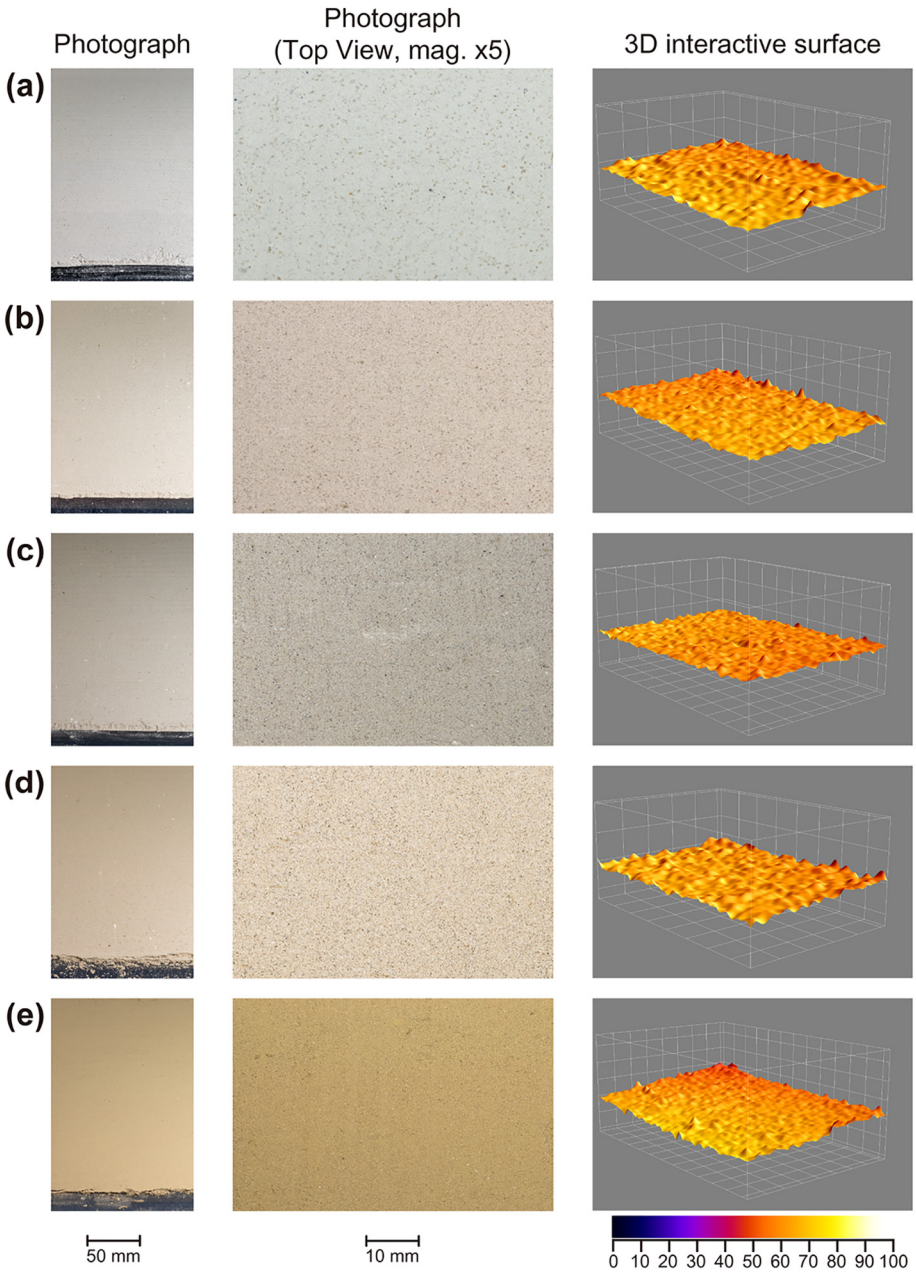

Fig. 5. Photographs and 3D interactive surfaces of geopolymer powders with different slag/fly ash ratios: (a) S100FA0, (b) S75FA25 (c) S50FA50 (d) S25FA75 and (e) S0FA100.

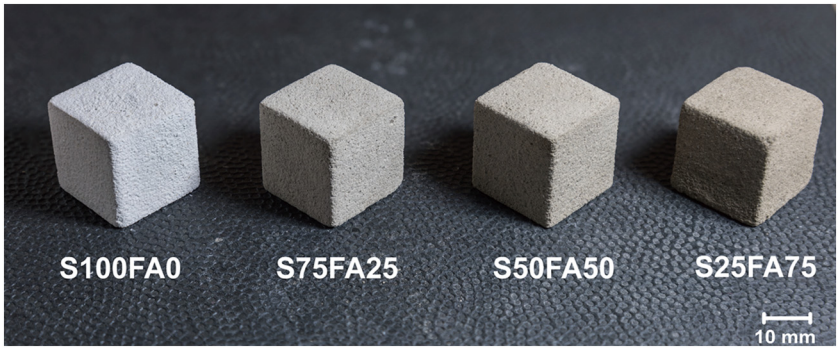

Fig. 6. Powder-based 3D printed green cubes using geopolymer powders with different slag/fly ash ratios. (For interpretation of the references to colour in this figure legend, the reader is referred to the web version of this article.)

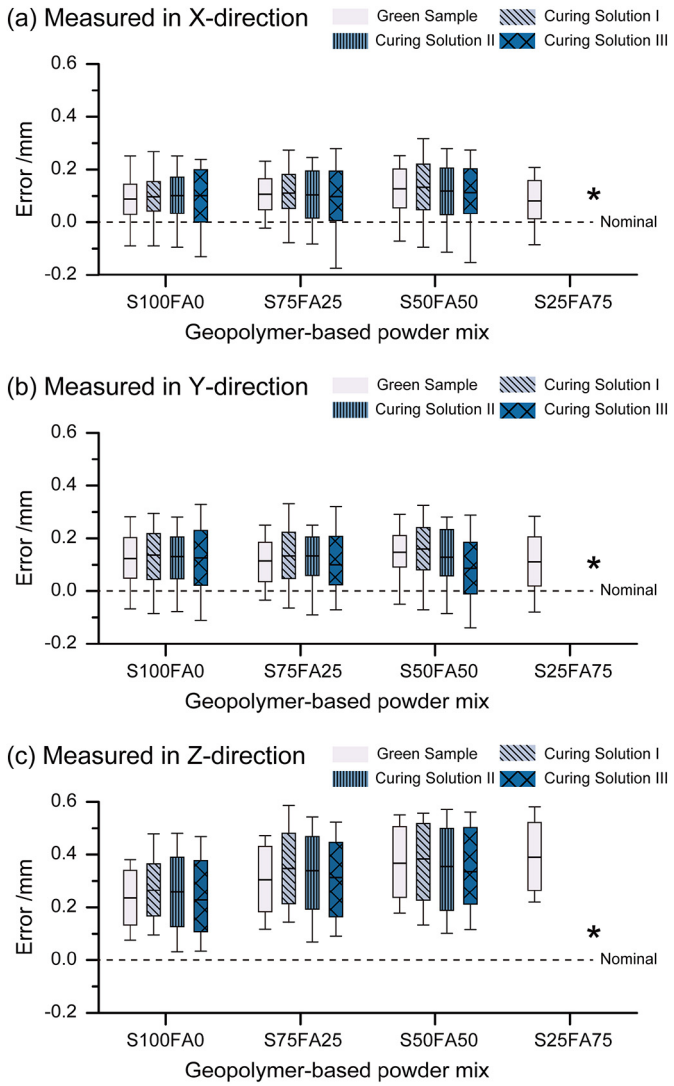

Fig. 7. Linear dimensional accuracy results of 3D printed cubes in (a) X-direction, (b) Y-direction and (c) *Z*-direction. (Box: Mean ± Standard deviation; Whisker: Minimum to Maximum). Note: *No data is available for S25FA75 post-processed samples as they were dissolved in the curing solutions.

in all directions. The pattern observed regarding the linear dimensional accuracy of the samples immersed in Curing Solution II was quite different from that of the samples immersed in Curing Solution I. In S100FA0 and S75FA25 samples, the mean error values in the X-direction and Y-direction were quite close to those of the green samples. Whereas, the mean error values in the *Z*-direction were higher than those of the green samples. On the other hand, in S50FA50 samples the mean error values were lower than those of the green samples in all directions. This indicates that the S50FA50 post-processed samples exhibited higher linear dimensional accuracy after being immersed in Curing Solution II, as compared to the S50FA50 green samples.

The S100FA0 samples immersed in Curing Solution III exhibited the smallest difference in the mean error values before and after the post-processing. This indicates that Curing Solution III had the least effect on the linear dimensional accuracy of S100FA0 samples. For the S75FA25 and S50FA50 samples immersed in Curing Solution III, the mean error values in the X-direction were quite close to those of the green samples. However, the mean error values in Y-direction and Z-direction were lower than those of the green samples. This indicates that Curing Solution III improved the linear dimensional accuracy in these two directions.

Among the alkaline solutions investigated in this study for the post-processing, the samples immersed in Curing Solution III exhibited the lowest mean error values, thereby the highest linear dimensional accuracy in all directions. This is true regardless of the fly ash content. This may be attributed to the polymerization of the oligomeric silica species in the aqueous phase and the viscosity of curing solutions. During the post-processing process, silicate species existed in curing solutions aggregate and form a uniform 3D network of silicate particles [47]. When polymerization begins, the silicate gel precipitates on the surface of the immersed sample causing the increase in the linear dimensions.

In sodium silicate solutions, lowering the pH for a certain silicate content reduces the time of polycondensation [47]. Among the three curing solutions investigated in this study, Curing Solution I had the lowest alkalinity, more silicate gel from the aqueous phase precipitated on the surfaces of the immersed sample. With regards to Curing Solution II, addition of the NaOH solution increased the alkalinity and polymerization time; thereby less silicate gel precipitated on the immersed sample's surfaces.

According to Yang et al. [48], Curing Solution III ($nSiO_2/nNa_2O = 1.84$) had lower viscosity compared to Curing solution I ($nSiO_2/nNa_2O = 0.9$) and Curing Solution II ($nSiO_2/nNa_2O = 0.57$). The lower viscosity of Curing Solution III makes it easier to penetrate inside the immersed sample, which favors the geopolymerisation reaction. The higher amount of soluble silica in Curing Solution III also accelerates the rate of geopolymerisation reaction. Thereby, more chemical shrinkage was induced in the samples immersed in Curing Solution III. In the meantime, the higher alkalinity of Curing Solution III causes less silicate gel precipitation. Thus, it is reasonable that the samples immersed in Curing Solution III exhibited the lowest mean error values.

3.2.2. Mechanical property analysis

The seven-day uniaxial compressive strengths of both green and post-processed 3D printed cubes are presented in Fig. 8. As mentioned before, S25F75 samples were dissolved in the curing solutions during the post-processing process. Therefore, no data is available for the compressive strength of S25FA75 post-processed samples.

3.2.2.1. Mechanical property analysis of green samples. As shown in Fig. 8, the green samples exhibited relatively low compressive strength ranging from 0.24 to 0.91 MPa, depending on the testing direction and fly ash content. However, it is necessary to note that this strength level was already sufficient for the de-powdering process.

In both directions, the increase of fly ash content significantly decreased the compressive strength of the green samples. This is attributed to the low reactivity of fly ash at ambient temperature.

An anisotropic phenomenon was also observed regarding the compressive strength of the green samples depending on the loading directions. Regardless of the content of fly ash, the compressive strength was always higher in the X-direction than in the *Z*-direction.

The green compressive strength of S100FA0, S75FA25, S50FA50 and S25FA75 samples in the X-Direction were 20%, 25%, 41% and 42%, respectively higher than that of the corresponding samples in the Z-Direction. In other words, for the green samples $f_{c\text{-}x}/f_{c\text{-}z}$ ratio increased from 1.20 to 1.42 when the fly ash content increased from 0% to 75%. The possible reason for this anisotropy in compressive strength can be explained as follows:

Fly ash does not react with the alkaline activator at ambient temperature. However, it affects the droplet penetration depth as listed in Table 5. According to Lowke et al. [49], in the green samples, the water content significantly oscillates in accordance with a higher water content in the top region of the layer and a significantly lower content in the bottom region. The intralayer water gradient will be minimized by increasing the droplet penetration depth, and the interlayer bond will be enhanced. Therefore, the degree of anisotropy may be attributed to

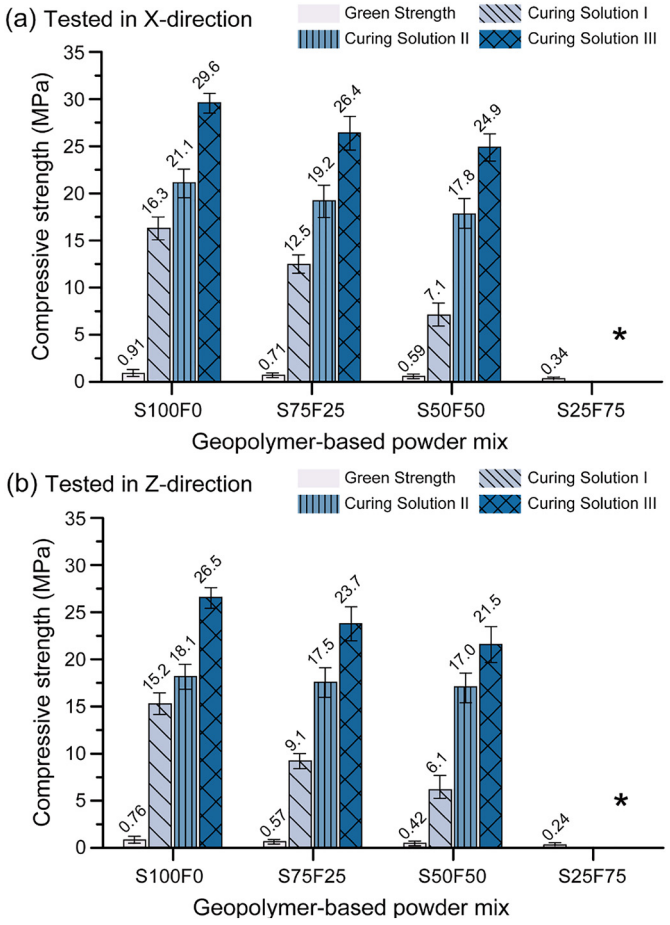

Fig. 8. The seven-day uniaxial compressive strength of both green and post-processed 3D printed cubes measured in (a) X-Direction, (b) *Z*-Direction. Note: *No data is available for S25FA75 post-processed samples as they were dissolved in the curing solutions. (For interpretation of the references to colour in this figure legend, the reader is referred to the web version of this article.)

the droplet penetration depth, which changes the quality of interlayer bond; actually the penetration depth, according to the results presented in Table 5, is subject to fly ash content.

3.2.2.2. Mechanical property analysis of post-processed samples. According to Fig. 8, in both directions the compressive strength of post-processed samples was significantly higher than that of the green samples. This is true regardless of the type of curing solutions. This is due to the continued geopolymerisation process as a result of immersion of the samples for seven days in the alkaline solutions. More geopolymeric products were formed and developed, resulting in the densification of porous structures of the green samples.

Similar to the compressive strength of the green samples, there was an anisotropic phenomenon regarding the compressive strength of the post-processed samples depending on the loading directions. Irrespective of the fly ash content, the compressive strength of the post-processed samples was always higher in the X-direction than in the *Z*-direction.

Regardless of the testing direction and type of curing solution, S100FA0 samples always exhibited the highest post-processed compressive strength. The increase of fly ash content decreased the compressive strength of the post-processed samples in both directions. However, the rate of reduction in the compressive strength depended on the type of curing solutions, with the highest reduction rate being for Curing Solution I. The post-processed compressive strength of S75FA25 and S50FA50 samples being immersed in Curing Solution I were 23–56% and 40–60%, respectively lower than that of S100FA0 samples depending on the testing direction. This is attributed to the low alkalinity of Curing Solution I. During the dissolution of geopolymer precursors, the hydroxide ions (OH^-) act as a reaction catalyst [29]. Compared with slag, the dissolution of silica and alumina species in fly ash particles requires a higher concentration of hydroxide ions. In Curing Solution I, the concentration of OH^- ions was insufficient to promote the geopolymerisation of all fly ash particles. Therefore, some of the fly ash particles acted as fillers and had not much effect on the development of the compressive strength of S75FA25 and S50FA50 samples.

On the other hand, the post-processed compressive strength of S75FA25 and S50FA50 samples being immersed in Curing Solution II were only 3–9% and 6–16%, respectively lower than that of S100FA0 samples depending on the testing direction. A similar pattern was observed when Curing Solution III was used. This is because the 8.0 M NaOH solution in Curing Solution II and III provided a stronger alkaline environment, which promoted the dissolving and surface hydrolysis of the fly ash particles, thereby enhancing the compressive strength development of S75FA25 and S50FA50 samples.

According to Fig. 8, Curing Solution III was the most effective in increasing the compressive strength among the curing solutions investigated in this study. The seven-day compressive strength of the samples immersed in Curing Solution III was in the range of 21.5 MPa to 29.6 MPa, depending on the fly ash content and testing direction, meeting the compressive strength requirements for many applications in the construction industry.

It is interesting to note that the compressive strengths of S100FA0, S75FA25 and S50FA50 samples immersed in Curing Solution III were 40–46%, 35–38%, and 27–40%, respectively higher than those of the samples immersed in Curing Solution II. This is because instead of saturated anhydrous sodium metasilicate solution (with SiO_2/Na_2O molar ratio of 0.9) in Curing Solution II, Curing Solution III contained N Grade sodium silicate solution (with SiO_2/Na_2O molar ratio of 3.22), which provides higher amount of soluble silica in the curing solutions. This in turn accelerates the rate of geopolymerisation reaction, thereby improves the compressive strength [50].

3.3. The merits and demerits of the approach

The approach described above uses a powder-based 3DCP for construction applications. The merits of this system have been described in Section I (Introduction). The main demerit is that this approach can only make small building elements due to the size limitation of the printer at this stage of the technology.

Previous researchers have developed conventional cement systems for the powder-based 3DCP process. The main advantages of using geopolymer system over conventional cement systems are also described in Section I (Introduction). The main disadvantage of using geopolymer system developed in this study is the need for heat curing in an alkaline solution which is an additional requirement.

The previous approach developed by the authors of this study [24. 25] used slag only for the geopolymer precursor. The current approach presented in this paper is formulated using fly ash and slag with different mass ratios. The main merit of introducing the fly ash in the approach is that fly ash is more abundantly available and large parts of it is still dumped in many parts of the world as compared to slag. While slag is also an industrial by-product, it has higher utilization rate in the concrete industry. The main demerit of using fly ash in this approach is that it requires stronger alkaline environment and the “green” strength is also lower than the slag only approach.

4. Conclusions

The influence of incorporation of fly ash on the properties of powder-based 3D printable geopolymer was investigated in this study.

It is intended to expand the scope of geopolymer materials that can be used in the powder-based 3DCP process for construction applications. Five geopolymer powders with different slag to fly ash ratios were used in a commercially available powder-based 3D printer. The effect of different amounts of fly ash (0, 25, 50, 75, and 100 wt%) on depositability and wettability of the geopolymer powder, along with the dimensional accuracy and compressive strength of the printed specimens were quantitatively evaluated. For the post-processing, the green specimens were immersed in three different alkaline solutions. The influence of type of alkaline solution on the dimensional accuracy and compressive strength of the post-processed specimens were investigated. The following specific conclusions can be drawn from this study:

(1) The minimum amount of slag required to prepare fly ash/slag blended geopolymer powder for powder-based 3DCP process was 50 wt%. The 7-day compressive strength of up to 24.9 MPa was achieved for the post-processed specimens printed with 50 wt% slag/50 wt% fly ash powder. The specimens printed with the geopolymer powders containing less than 50 wt% slag (i.e. more than 50 wt% fly ash) either did not have enough green strength to resist the de-powdering process, or were dissolved in the curing solutions during the post-processing process. This is due to the low reactivity of these powders with the binder liquid at ambient temperature.
(2) The specimens printed with 100% slag-based geopolymer powder always exhibited the highest green and post-processed compressive strengths. This is true regardless of the testing direction and type of curing solution. The increase of fly ash content decreased the compressive strength of both green and post-processed samples in both directions. The lower compressive strength of the green samples with higher fly ash content is attributed to the low reactivity of fly ash at ambient temperature. The rate of reduction in the compressive strength of post-processed samples due to increase in fly ash content depended on the type of curing solution, with the highest reduction rate being for Curing Solution I composed of saturated anhydrous sodium metasilicate solution with SiO_2/Na_2O molar ratio of 0.9 (100% *w*/w). This is attributed to the low alkalinity of Curing Solution I, as compared to the other two curing solutions.
(3) Among the curing solutions investigated, Curing Solution III composed of N Grade sodium silicate solution with SiO_2/Na_2O molar ratio of 3.22 (71.4% w/w) and 8.0 M NaOH solution (28.6% w/w) was the most effective in increasing the compressive strength of the printed specimens. This is because Curing Solution III provided a higher amount of soluble silica and alkalinity as compared to the other two curing solutions, which in turn promoted the dissolving and surface hydrolysis of the fly ash particles and accelerated the rate of geopolymerisation reaction. The seven-day compressive strength of the samples immersed in Curing Solution III was in the range of 21.5 MPa to 29.6 MPa, depending on the fly ash content and testing direction, which meets the compressive strength requirements for many applications in the construction industry.
(4) The compressive strength of the printed samples exhibited orthotropic properties depending on the loading directions. The compressive strengths of both green and post-processed specimens were always higher in the X-direction than in the *Z*-direction. This is true regardless of the fly ash content. This anisotropy may be related to the preferential orientation of the powder particles during the powder spreading process.
(5) An anisotropic phenomenon was observed regarding the linear dimensional accuracy of the green samples depending on the direction. The X-direction had the highest linear dimensional accuracy. This is true regardless of the fly ash content. This might be because the X-direction (i.e., the binder jetting direction) is not affected by the powder spreading, which takes place in the Y-direction. The increase of the fly ash content significantly reduced the linear dimensional accuracy of the green samples in the Z-direction, which could be attributed to the differences in powder bed structure and level of powder/binder reactivity of the geopolymer powders. On the other hand, the fly ash content had a minor effect on the linear dimensional accuracy in the X-direction and Y-direction.
(6) The post-processed specimens also exhibited an anisotropic phenomenon regarding the linear dimensional accuracy depending on the curing solution and testing direction. Among the curing solutions investigated, the samples immersed in Curing Solution III, regardless of the fly ash content, exhibited the highest dimensional accuracy in all directions. This could be attributed to the polymerization of the oligomeric silica species in the aqueous phase and viscosity of the curing solutions.
(7) The increase of the fly ash content increased the binder droplet penetration time. This is because the higher amount of fly ash reduced the average particle size of the geopolymer powder, thereby increased the time needed for the binder droplet to completely penetrate into the powder bed. The higher fly ash content increased the spreading diameter of the binder droplet, but reduced the binder droplet penetration depth. This may be attributed to the reduction in the powder bed surface hydrophilicity, resulting from the reduction in the average particle size of the powder.
(8) The amount of fly ash did not have any significant effect on the true, bulk and in-process bed densities and powder bed porosity of the 3D printable geopolymer powders. Visual observations revealed that all geopolymer powders exhibited sufficient surface qualities for the powder-based 3DCP process.

Acknowledgments

Authors acknowledge the support by the Australian Research Council Discovery Grant DP170103521 and Linkage Infrastructure Grant LE170100168 and Discovery Early Career Researcher Award DE180101587.

References

[1] T. Wohlers, Wohlers Report 2016, Wohlers Associates, Inc, 2016 (ISBN 978-0-9913332-2-6).
[2] R.A. Buswell, A. Thorpe, R.C. Soar, A.G.F. Gibb, Design, data and process issues for mega-scale rapid manufacturing machines used for construction, Autom. Constr. 17 (2008) 923–929, https://doi.org/10.1016/j.autcon.2008.03.001.
[3] S. Lim, R.A. Buswell, T.T. Le, S.A. Austin, A.G. Gibb, T. Thorpe, Developments in construction-scale additive manufacturing processes, Autom. Constr. 21 (2012) 262–268, https://doi.org/10.1016/j.autcon.2011.06.010.
[4] B. Khoshnevis, Automated construction by contour crafting-related robotics and information technologies, Autom. Constr. 13 (2004) 5–19, https://doi.org/10.1016/j.autcon.2003.08.012.
[5] B. Nematollahi, M. Xia, J. Sanjayan, Current progress of 3D concrete printing technologies, ISARC, Proceedings of the International Symposium on Automation and Robotics in Construction, Taipei, 2017, https://doi.org/10.22260/ISARC2017/0035.
[6] B. Zareiyan, B. Khoshnevis, Effects of interlocking on interlayer adhesion and strength of structures in 3D printing of concrete, Autom. Constr. 83 (2017) 212–221, https://doi.org/10.1016/j.autcon.2017.08.019.
[7] Y.W.D. Tay, B. Panda, S.C. Paul, N.A. Noor Mohamed, M.J. Tan, K.F. Leong, 3D printing trends in building and construction industry: a review, Virtual Phys. Prototyping 12 (2017) 261–276, https://doi.org/10.1080/17452759.2017.1326724.
[8] Y.W.D. Tay, G.H.A. Ting, Y. Qian, B. Panda, L. He, M.J. Tan, Time gap effect on bond strength of 3D-printed concrete, Virtual Phys. Prototyping (2018) 1–10, https://doi.org/10.1080/17452759.2018.1500420.
[9] Y. Weng, M. Li, M.J. Tan, S. Qian, Design 3D printing cementitious materials via fuller Thompson theory and Marson-Percy model, Constr. Build. Mater. 163 (2018) 600–610, https://doi.org/10.1016/j.conbuildmat.2017.12.112.
[10] J.G. Sanjayan, B. Nematollahi, M. Xia, T. Marchment, Effect of surface moisture on inter-layer strength of 3D printed concrete, Constr. Build. Mater. 172 (2018) 468–475, https://doi.org/10.1016/j.conbuildmat.2018.03.232.
[11] B. Nematollahi, P. Vijay, J. Sanjayan, A. Nazari, M. Xia, V. Naidu Nerella, V. Mechtcherine, Effect of polypropylene fibre addition on properties of geopolymers made by 3D printing for digital construction, Materials 11 (2018) 2352, https://doi.org/10.3390/ma11122352.
[12] B. Nematollahi, M. Xia, J. Sanjayan, P. Vijay, Effect of type of fiber on inter-layer bond and flexural strengths of extrusion-based 3D printed geopolymer, Mater. Sci.

Forum 939 (2018) 155–162, https://doi.org/10.4028/www.scientific.net/MSF.939.155.
[13] G. Cesaretti, E. Dini, X. De Kestelier, V. Colla, L. Pambaguian, Building components for an outpost on the lunar soil by means of a novel 3D printing technology, Acta Astronaut. 93 (2014) 430–450, https://doi.org/10.1016/j.actaastro.2013.07.034.
[14] R. Rael, V. San Fratello, Developing concrete polymer building components for 3D printing, ACADIA, 31st Annual Conference of the Association for Computer Aided Design in Architecture, Banff, 2011 http://www.rael-sanfratello.com/media/emerging_objects/papers/243.pdf , Accessed date: 17 December 2018.
[15] D. Dimitrov, W. Van Wijck, K. Schreve, N. De Beer, Investigating the achievable accuracy of three dimensional printing, Rapid Prototyp. J. 12 (2006) 42–52, https://doi.org/10.1108/13552540610637264.
[16] P.-H. Lee, H. Chung, S.W. Lee, J. Yoo, J. Ko, Review: dimensional accuracy in additive manufacturing processes, ASME 2014 international manufacturing science and engineering conference collocated with the JSME 2014 international conference on materials and processing and the 42nd north American manufacturing research conference, Am. Soc. Mech. Eng. (2014), https://doi.org/10.1115/MSEC2014-4037 (pp. V001T004A045-V001T004A045).
[17] S. Lim, R.A. Buswell, T.T. Le, R. Wackrow, S.A. Austin, A.G. Gibb, T. Thorpe, Development of a viable concrete printing process, 28th International Symposium on Automation and Robotics in Construction (ISARC2011), Seoul, 2011, pp. 665–670, , https://doi.org/10.22260/ISARC2011/0124.
[18] M. Xia, B. Nematollahi, J. Sanjayan, Compressive strength and dimensional accuracy of portland cement mortar made using powder-based 3D printing for construction applications, RILEM International Conference on Concrete and Digital Fabrication, Springer, 2018, pp. 245–254, , https://doi.org/10.1007/978-3-319-99519-9_23.
[19] M. Xia, B. Nematollahi, J. Sanjayan, Influence of binder saturation level on compressive strength and dimensional accuracy of powder-based 3D printed geopolymer, Mater. Sci. Forum 939 (2018) 177–183, https://doi.org/10.4028/www.scientific.net/MSF.939.177.
[20] B. Panda, Y. Tay, S. Paul, M. Tan, Current challenges and future potential of 3D concrete printing: aktuelle herausforderungen und zukunftspotenziale des 3D-druckens bei beton, Mater. Werkst. 49 (2018) 666–673, https://doi.org/10.1002/mawe.201700279.
[21] J.J. Biernacki, J.W. Bullard, G. Sant, K. Brown, P. Fredrik, S. Jones Glasser, et al., Cements in the 21st century: challenges, perspectives, and opportunities, J. Am. Ceram. Soc. 100 (2017) 2746–2773, https://doi.org/10.1111/jace.14948.
[22] G.J. Gibbons, R. Williams, P. Purnell, E. Farahi, 3D printing of cement composites, Adv. Appl. Ceram. 109 (2010) 287–290, https://doi.org/10.1179/174367509X12472364600878.
[23] A.K. Maier, L. Dezmirean, J. Will, P. Greil, Three-dimensional printing of flash-setting calcium aluminate cement, J. Mater. Sci. 46 (2011) 2947–2954, https://doi.org/10.1007/s10853-010-5170-4.
[24] M. Xia, J. Sanjayan, Method of formulating geopolymer for 3D printing for construction applications, Mater. Des. 110 (2016) 382–390, https://doi.org/10.1016/j.matdes.2016.07.136.
[25] M. Xia, J.G. Sanjayan, Methods of enhancing strength of geopolymer produced from powder-based 3D printing process, Mater. Lett. 227 (2018) 281–283, https://doi.org/10.1016/j.matlet.2018.05.100.
[26] B. Nematollahi, J. Qiu, E.-H. Yang, J. Sanjayan, Microscale investigation of fiber-matrix interface properties of strain-hardening geopolymer composite, Ceram. Int. 43 (2017) 15616–15625, https://doi.org/10.1016/j.ceramint.2017.08.118.
[27] B. Nematollahi, J. Sanjayan, F.U.A. Shaikh, Synthesis of heat and ambient cured one-part geopolymer mixes with different grades of sodium silicate, Ceram. Int. 41 (2015) 5696–5704, https://doi.org/10.1016/j.ceramint.2014.12.154.
[28] B. Nematollahi, J. Qiu, E.-H. Yang, J. Sanjayan, Micromechanics constitutive modelling and optimization of strain hardening geopolymer composite, Ceram. Int. 43 (2017) 5999–6007, https://doi.org/10.1016/j.ceramint.2017.01.138.
[29] P. Duxson, A. Fernández-Jiménez, J.L. Provis, G.C. Lukey, A. Palomo, J.S.J. Deventer, Geopolymer technology: the current state of the art, J. Mater. Sci. 42 (2006) 2917–2933, https://doi.org/10.1007/s10853-006-0637-z.
[30] P. Duxson, J.L. Provis, G.C. Lukey, J.S. Van Deventer, The role of inorganic polymer technology in the development of 'green concrete', Cem. Concr. Res. 37 (2007) 1590–1597, https://doi.org/10.1007/s10853-006-0637-z.
[31] S.H. Bong, B. Nematollahi, A. Nazari, M. Xia, J.G. Sanjayan, Fresh and hardened properties of 3D printable geopolymer cured in ambient temperature, RILEM International Conference on Concrete and Digital Fabrication, Springer, 2018, pp. 3–11, , https://doi.org/10.1007/978-3-319-99519-9_1.
[32] B. Nematollahi, M. Xia, S.H. Bong, J. Sanjayan, Hardened properties of 3D printable 'one-part' geopolymer for construction applications, RILEM International Conference on Concrete and Digital Fabrication, Springer, 2018, pp. 190–199, , https://doi.org/10.1007/978-3-319-99519-9_17.
[33] M. Asadi-Eydivand, M. Solati-Hashjin, S.S. Shafiei, S. Mohammadi, M. Hafezi, N.A.A. Osman, Structure, properties, and in vtro behavior of heat-treated calcium sulfate scaffolds fabricated by 3D printing, PLoS One 11 (2016) e0151216, , https://doi.org/10.1371/journal.pone.0151216.
[34] Y. Shanjani, E. Toyserkani, Material spreading and compaction in powder-based solid freeform fabrication methods: mathematical modeling, 19th Annual International Solid Freeform Fabrication Symposium, SFF 2008, 2008, pp. 399–410 http://edge.rit.edu/edge/P10551/public/SFF/SFF%202008%20Proceedings/Manuscripts/2008-36-Shanjani.pdf , Accessed date: 17 December 2018.
[35] B. Utela, D. Storti, R. Anderson, M. Ganter, A review of process development steps for new material systems in three dimensional printing (3DP), J. Manuf. Process. 10 (2008) 96–104, https://doi.org/10.1016/j.jmapro.2009.03.002.
[36] B.R. Utela, D. Storti, R.L. Anderson, M. Ganter, Development process for custom three-dimensional printing (3DP) material systems, J. Manuf. Sci. E. T. ASME 132 (2010) 0110081–0110089, https://doi.org/10.1115/1.4000713.
[37] D.L. Kong, J.G. Sanjayan, K. Sagoe-Crentsil, Comparative performance of geopolymers made with metakaolin and fly ash after exposure to elevated temperatures, Cem. Concr. Res. 37 (2007) 1583–1589, https://doi.org/10.1016/j.cemconres.2007.08.021.
[38] C. Tennakoon, A. Nazari, J.G. Sanjayan, K. Sagoe-Crentsil, Distribution of oxides in fly ash controls strength evolution of geopolymers, Constr. Build. Mater. 71 (2014) 72–82, https://doi.org/10.1016/j.conbuildmat.2014.08.016.
[39] K.P. Hapgood, J.D. Litster, S.R. Biggs, T. Howes, Drop penetration into porous powder beds, J. Colloid Interface Sci. 253 (2002) 353–366, https://doi.org/10.1006/jcis.2002.8527.
[40] K. Lu, M. Hiser, W. Wu, Effect of particle size on three dimensional printed mesh structures, Powder Technol. 192 (2009) 178–183, https://doi.org/10.1016/j.powtec.2008.12.011.
[41] E. Nefzaoui, O. Skurtys, Impact of a liquid drop on a granular medium: inertia, viscosity and surface tension effects on the drop deformation, Exp. Thermal Fluid Sci. 41 (2012) 43–50, https://doi.org/10.1016/j.expthermflusci.2012.03.007.
[42] A.L. Mundozah, J.J. Cartwright, C.C. Tridon, M.J. Hounslow, A.D. Salman, Hydrophobic/hydrophilic static powder beds: competing horizontal spreading and vertical imbibition mechanisms of a single droplet, Powder Technol. 330 (2018) 275–283, https://doi.org/10.1016/j.powtec.2018.02.032.
[43] H. Li, J. Zhang, Y. Zhao, C.-Y. Wu, C. Zheng, Wettability of fly ashes from four coal-fired power plants in China, Ind. Eng. Chem. Res. 50 (2011) 7763–7771, https://doi.org/10.1021/ie2001378.
[44] G.A. Fielding, A. Bandyopadhyay, S. Bose, Effects of silica and zinc oxide doping on mechanical and biological properties of 3D printed tricalcium phosphate tissue engineering scaffolds, Dent. Mater. 28 (2012) 113–122, https://doi.org/10.1016/j.dental.2011.09.010.
[45] A. Farzadi, M. Solati-Hashjin, M. Asadi-Eydivand, N.A.A. Osman, Effect of layer thickness and printing orientation on mechanical properties and dimensional accuracy of 3D printed porous samples for bone tissue engineering, PLoS One 9 (2014), https://doi.org/10.1371/journal.pone.0108252.
[46] Y. Shanjani, Y. Hu, R.M. Pilliar, E. Toyserkani, Mechanical characteristics of solid-freeform-fabricated porous calcium polyphosphate structures with oriented stacked layers, Acta Biomater. 7 (2011) 1788–1796, https://doi.org/10.1016/j.actbio.2010.12.017.
[47] A.A. Hamouda, H.A.A. Amiri, Factors affecting alkaline sodium silicate gelation for in-depth reservoir profile modification, Energies 7 (2014) 568–590, https://doi.org/10.3390/en7020568.
[48] X. Yang, W. Zhu, Q. Yang, The viscosity properties of sodium silicate solutions, J. Solut. Chem. 37 (2008) 73–83, https://doi.org/10.1007/s10953-007-9214-6.
[49] D. Lowke, E. Dini, A. Perrot, D. Weger, C. Gehlen, B. Dillenburger, Particle-bed 3D printing in concrete construction–possibilities and challenges, Cem. Concr. Res. 112 (2018) 50–65, https://doi.org/10.1016/j.cemconres.2018.05.018.
[50] H. Xu, J.S.J. Van Deventer, The geopolymerisation of alumino-silicate minerals, Int. J. Miner. Process. 59 (2000) 247–266, https://doi.org/10.1016/S0301-7516(99)00074-5.